

High-uniformity magnetic field configurations for trapped ions and optical verification

Nelson Ooi*

Advised by Professor Karan Mehta
Research sponsored by James Moore '62 EE fund

August 18, 2023

Abstract

Trapped-ion quantum devices utilize the quantum mechanical behavior of atomic ions to perform computational tasks. Current systems generally require stable, high-uniformity magnetic fields and low-noise EM signals to avoid the introduction of undesirable perturbations. We discuss techniques to create permanent magnet configurations and high-coherence laser systems to achieve these goals.

1 Introduction

Trapped-ion architectures are a leading approach for implementing quantum information processors, due to the long qubit coherence times and high-fidelity operations offered by this platform [1–3]. Information can be encoded in ion qubits using discrete energy levels with transitions driven by lasers operating at optical or IR frequencies [4–6]. To create well-defined, addressable energy sublevels, it is generally useful to apply a quantizing magnetic field that lifts the degeneracies in an ion qubit’s Zeeman manifolds [7–9].

Gradients in the applied magnetic field can cause in undesirable decoherence effects in ion qubits. Transporting an ion qubit through a spatially-varying magnetic field causes dephasing via an accrual of ‘noisy’ relative phase in the qubit’s internal state, thereby distorting the encoded information with little recourse for recovery [10]. Magnetic field fluctuations can furthermore cause shifts in qubit energy levels via the Zeeman effect, skewing state transition resonance frequencies: Schmidt-Kaler et. al. state that a 1mG fluctuation can cause a 4.2kHz shift in the $^{40}\text{Ca}^+$ carrier frequency [11]. Magnetic field fluctuations and nonuniformity can therefore pose a significant constraint on qubit coherence times.

*School of Electrical and Computer Engineering, College of Engineering, Cornell University, Ithaca, New York, USA. Email: no83@cornell.edu

Recent approaches to avoid decoherence induced by magnetic inhomogeneities include magnetic shielding using μ -metal enclosures, and using permanent magnets for quantizing field generation in place of inductive magnetic sources [2,12,13]. Permanent magnet configurations do not suffer the same drawbacks as current-driven sources, such as ohmic heating effects that adversely increase heat load on cryogenic apparatus as well as direct current fluctuations which introduce undesirable magnetic field noise [12]. It is therefore of interest to create permanent magnet geometries that provide a target quantizing field strength at low magnetic field nonuniformity. When used in conjunction with the above approaches, this has the potential to mitigate qubit dephasing.

Presently, a number of magnetic geometries have been explored to generate homogenous magnetic fields for sensor calibration and magnetic resonance imaging (MRI) [14,15]. These include electromagnetic systems, such as Helmholtz, Maxwell coils and n-coil configurations [14,16,17], and also permanent magnet systems, including the Halbach cylinder and its derivatives [18–20]. We draw upon approaches to formulate and devise a new approach to optimizing the permanent magnet geometries.

In this paper, we demonstrate and compare efficient computational approaches to optimize permanent magnet geometries to create high uniformity magnetic fields for trapped-ion quantum computing applications. Using these numerical schemes, we demonstrate designs with average magnetic field strength nonuniformity on the order of 0.1ppm or better over the desired region of interest, complemented by target field strengths on the order of 10G. We also outline challenges posed by manufacturing variations in generating high uniformity fields for trapped-ion quantum devices, and assess these effects on permanent magnet performance.

As a next step, we aim to fabricate these high-homogeneity permanent magnet geometries and measure the resultant B-field gradient achieved in practice within the overall cryogenic chamber setup. With the method outlined by Walther et. al. [21], a single $^{40}\text{Ca}^+$ ion may be used to map magnetic field magnitude gradients with high spatial resolution. A key element of this detection scheme, and of ensuring long coherence times for ion qubits in general, is that lasers require stable and narrow linewidths. We achieve this in our setup using frequency locking via the Pound-Drever-Hall technique [22], and via the optical fiber noise cancellation technique described by Ma et. al. [23].

In the second part of this paper, we present the design and experimental setup of a fiber-noise cancellation (FNC) laser system based on the Ma et. al. scheme [23], further inspired by recent implementations [13,24,25]. A bill of materials (BOM) for this setup is provided in the relevant section.

2 Methods for magnetic field optimization

2.1 Establishing optimization targets

We first outline the target performance figures for a successful permanent magnet geometry. Three key metrics are used, namely: the magnetic field strength in the chosen region of interest, the degree of magnetic field homogeneity over the region of interest, and the spatial

extent of the region with homogenous field.

2.1.1 Target magnetic field strength

$^{40}\text{Ca}^+$ is among the most widely-studied ion qubit species for trapped-ion quantum computing applications. Prior trapped-ion experiments using $^{40}\text{Ca}^+$ have utilized magnetic field strengths on the order of 2.4 – 5.9G to split degenerate energy levels via the Zeeman effect [11–13]. Based on the Zeeman splitting per unit magnetic field in $^{40}\text{Ca}^+$ [26], a field strength of 10G can prevent overlaps in the relevant $S \rightarrow D$ transition frequencies to ensure that populations are excited to the appropriate sublevel (Y. Motohashi, personal communication, July 14, 2023). We therefore target a nominal magnetic field strength of 10G with our permanent magnet geometry.

2.1.2 Target degree of homogeneity

The magnetic field strength dependence of transition frequencies used in commonly-used ion qubits, i.e. $^{40}\text{Ca}^+$ or $^9\text{Be}^+$, typically occurs on the order of $\sim 1\text{MHz/G}$ [5,11,26]. We define stable qubit transition frequencies over the region of interest as having variations of $\sim 1\text{Hz}$. As such, magnetic field strength variation of $\sim 10^{-6}\text{G}$ over the region of interest is required. This is equivalent to an average magnetic field nonuniformity of $\sim 0.1\text{ppm}$ considering the 10G magnetic field strength outlined previously.

In our chosen coordinate system, the region of interest (ROI) lies in the $z = 0$ plane and the quantizing magnetic field intersects it perpendicularly, pointing along the z -axis. The planar ROI is centered on the origin, and we define the *point nonuniformity* at a point \mathbf{r} in the ROI as follows:

$$\eta_{ROI} = \left| \frac{B(\mathbf{r}) - B_0}{B_0} \right|$$

where $B(\mathbf{r})$ is the magnitude of the magnetic field strength at position \mathbf{r} in our coordinate system, and B_0 is the magnitude of the magnetic field strength at the origin (and is positive by definition) [17]. A more useful measure used for the optimization problem is the *average nonuniformity over the ROI*, which is represented by $\bar{\eta}_{ROI}$ and also interchangeably referred to hereafter as the ‘nonuniformity’ unless otherwise noted. The computation to obtain this value is covered in a later section.

2.1.3 Target spatial extent of homogeneity

The optimized region of interest (ROI) is defined by the surface area of a typical ion trap chip. Ions are typically shuttled across the extent of the trap surface, an area with dimensions on the order of 1cm by 1cm for contemporary designs [27–29], and it is essential to minimize qubit dephasing throughout the ion qubit transport process via the supply of a stable, homogenous magnetic field. Noting that the scale of trap chips is likely to grow with increasing qubit and module connections, we select an ROI measuring 2cm by 2cm in the $z = 0$ plane.

2.2 Optimization problem definition

We construct a multi-objective optimization problem to find appropriate dimensions for the permanent magnets that achieve the targets outlined previously.

The problem is defined as follows:

$$\min_{\mathbf{x}} : \bar{\eta}_{ROI} = \frac{1}{|A_{ROI}|} \iint_{A_{ROI}} \left| \frac{B(\mathbf{r}) - B_0}{B_0} \right| dx dy, \text{ and}$$

$$\Delta_B = |B_0 - 10|$$

s.t. \mathbf{x} is subject to geometry-specific bounds (see relevant sections for details).

where A_{ROI} is the area constituting the 2cm by 2cm region of interest, $\bar{\eta}_{ROI}$ is the average nonuniformity over the ROI, and \mathbf{x} is a vector of parameters describing each geometry.

2.2.1 Parameter bounds

The physical volume enclosed by the permanent magnet geometry is expected to be constrained by the size of typical cryogenic chambers used in trapped-ion experiments. Referring to dimensions from earlier work [12,13] and that of our lab's current cryogenic chamber, a cuboidal bound on the dimensions of the overall permanent magnet geometry is set, measuring 340mm \times 340mm \times 620mm. Specific dimensional bounds pertaining to each geometry are covered in the relevant sections that follow.

2.3 Choice of permanent magnet geometries

We select for permanent magnet geometries that have inherent structural symmetries. Such built-in symmetry ensures that the magnetic field strength in at least one coordinate axis over the region of interest is an even function. This enables the cancellation of all odd derivatives in the Taylor expansion of the field strength expression along this axis near the origin, similar to the process outlined in [17], thereby contributing to better homogeneity.

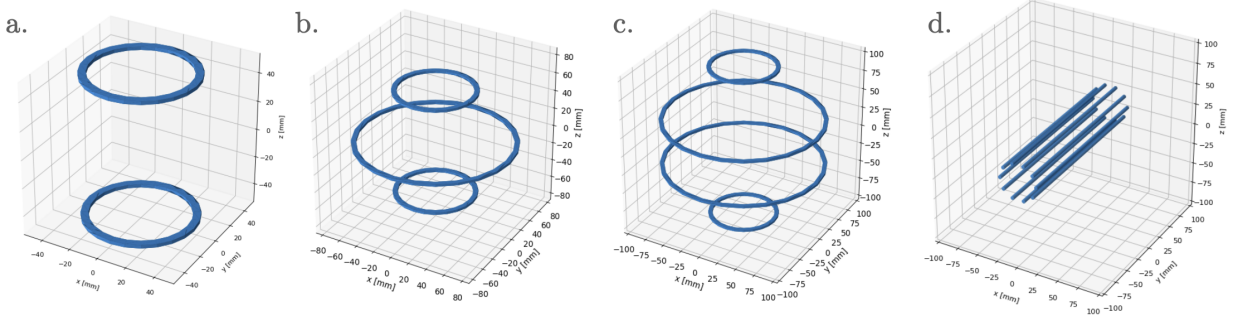


Figure 1: **a.** 2-ring geometry. **b.** 3-ring geometry. **c.** 4-ring geometry. Note that all rings are co-axial in the N-ring geometries. **d.** ‘Rod mangle’-type Halbach cylinder.

In all, four different permanent magnet geometries were chosen for optimization: N-rings (2, 3, 4), and the *rod mangle* type Halbach cylinder. A nominal example for each of the chosen geometries is shown in Figure 1.

2.3.1 N-ring geometries

The N-ring geometries (2, 3, 4-rings) are composed of symmetrical elements we call ‘ringsets’. Each ringset consists of a pair of rings, symmetric about the $z = 0$ plane. Within ringset i , the pair of rings share the same width (w_i in radial direction), thickness (t_i in z -direction), perpendicular distance from origin (d_i along z -direction), and inner radius (r_i), as shown in Figure 2. Note that d_i is measured from the midpoint of the thickness of each ring.

We count ringsets outwards from the origin, i.e. the closest ringset to the origin is denoted ringset 1, the next closest ringset 2, and so on. For instance, the 2-ring geometry consists of only one ringset, while 3 and 4-ring geometries have two ringsets. When the number of rings is odd, $d_1 = 0$ as ringset 1 is centered on the origin. The nearest pair of rings overlap fully, forming a single ring in ringset 1 as shown in Figure 2b.

All ringsets are positioned coaxially along the z -axis, and region of interest lies in the horizontal plane of symmetry. In our models, we study N-ring geometries with ring magnetization in the $+z$ -direction, through the ring thickness.

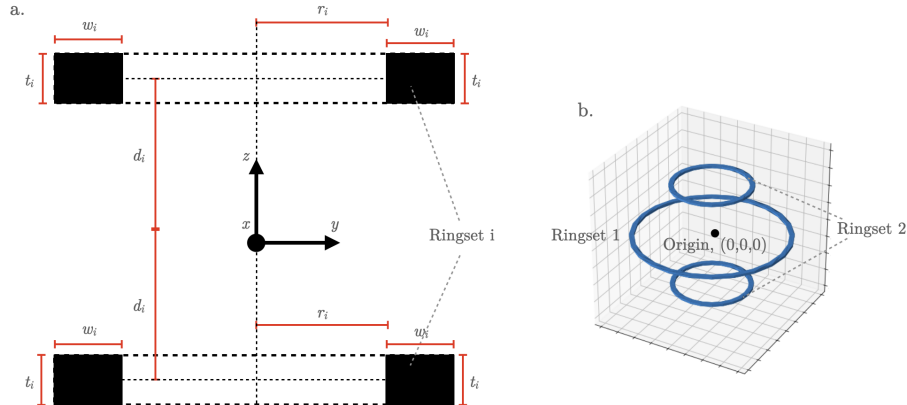


Figure 2: **a.** Cross-section of a coaxial ringset, with the relevant dimensional parameters labeled. **b.** Example of ringsets used in describing a 3-ring geometry: ringset 1 lies on the $z = 0$ plane and is the closest to the origin, while ringset 2 is the next closest.

For N-rings optimization, each dimension indicated in Figure 2 is constrained within the

following bounds for a ringset i , in units of mm.

$$1 < d_i < 300$$

$$1 < r_i < 150$$

$$2 < w_i < 20$$

$$2 < t_i < 20$$

2.3.2 Halbach cylinder geometry

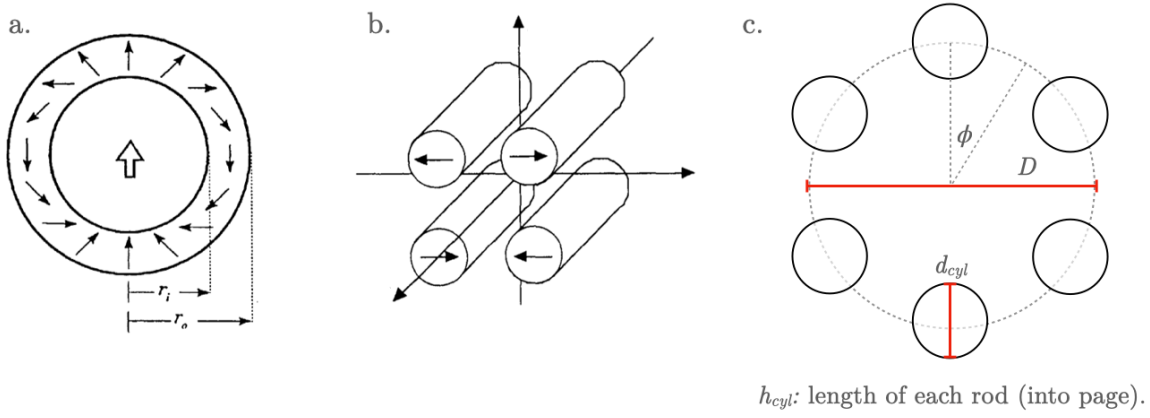


Figure 3: **a.** Continuous Halbach cylinder, with arrows in magnetic material denoting the direction of magnetization, and the arrow in the air-core denoting the direction of net homogenous magnetic field that is produced. The magnetic material extends into the page. Adapted from [30]. **b.** ‘Rod mangle’ discretization of Halbach cylinder, adapted from [31]. **c.** Diagram of $N = 6$ rod mangle structure with parameters relevant for our optimization model.

The Halbach cylinder is a permanent magnet geometry first proposed by Mallinson [32]. It is defined as a hollow cylinder with a wall constructed of magnetized material, whose magnetization axis varies as a function of angle. For specific wall magnetizations it is capable of generating strong, homogenous magnetic fields within its central air-core region [30]. The analytical expression for wall magnetization that results in greatest homogeneity is given as

$$\mathbf{B} = B_{rem} \left(\cos(\phi) \hat{\rho} + \sin(\phi) \hat{\phi} \right)$$

in polar coordinates, with the central magnetic field strength (in the ideal infinite length limit) given by

$$|\mathbf{B}| = B_{rem} \ln \left(\frac{r_o}{r_i} \right)$$

where r_o is the outer radius and r_i is the inner radius [33].

In practice, discretized ferromagnetic segments have been used to implement Halbach cylinders. Especially in the MRI research community, such geometries enable compact, homogenous

magnetic field sources for medical imaging [34,35]. We have chosen to use the *magic mangle* or *rod mangle* Halbach cylinder discretization [31], where the continuous cylinder wall is replaced with a set of extended rods magnetized across the diameter, each placed at uniform intervals along the circumference of the hollow cylinder (see Figure 3c.). For N rods, the magnetization angle of the i th rod is given by

$$\phi_i = \frac{720^\circ}{N} \cdot (i - 1)$$

taken relative to the z -axis corresponding to $\phi = 0^\circ$ [19].

The rod mangle structure is useful for several key reasons: (1) it provides better access into the open cylinder for input and readout from the trap chip located in the hollow cylinder core, and that (2) it can be constructed from identically-magnetized rods, which improves the ease of fabricating the structure.

For the rod mangle optimization, the dimensions indicated in Figure 3c are constrained within the following bounds, in units of mm.

$$\begin{aligned} 1 < d_{cyl} &< 20 \\ 21 < D &< 300 \end{aligned}$$

In our simulations, we fix $h_{cyl} = 640\text{mm}$, the maximum possible length along the longest axis of the bounding cuboid. This permits closer approximation to the infinite-length limit of the Halbach cylinder geometry. Optimization is performed over a range of N rods.

2.4 Comparison of objective function schemes

A key part of our investigation centers on finding suitable objective functions and optimization schemes to foster rapid convergence to the outlined targets of field strength and homogeneity over the ROI. Two optimization schemes were tested to assess their performance.

Pre-experimental sampling revealed that the Nelder-Mead algorithm used in these schemes can terminate on different result parameters depending on the initial guess provided. This suggests the presence of numerous local optima over the search domain. Therefore, repeated randomized initialization is necessary to search for solutions which approach the global optima.

2.4.1 Two-stage optimization scheme, a.k.a. *Pippin*

We propose a two-stage multiple-shot optimization scheme, named Pippin¹, with the following steps:

1. Generate n_{shots} random shots of starting parameter guesses for a chosen geometry. Each initial guess is a vector \mathbf{x}_0 with the i th element $x_{0,i}$ randomly drawn from the uniform distribution $U(a_i, b_i)$, where a_i and b_i are the minimum and maximum constraints imposed on the i th dimensional parameter.

¹Named after the hobbit from the Lord of the Rings. Particularly because there are plenty of magnetic rings being optimized.

2. **Stage 1 optimization.** Minimize \mathbf{x} (subject to geometry constraints) with the objective function $C_1(\mathbf{x})$ defined as a discretization of $\bar{\eta}_{ROI}$. Numerically, this is performed by taking the mean non-uniformity over 101×101 grid points on the $20\text{mm} \times 20\text{mm}$ ROI, giving us the discretized objective function:

$$C_1(\mathbf{x}) = \bar{\eta}_{ROI} = \frac{1}{101^2} \sum_{x=1}^{101} \sum_{y=1}^{101} \left| \frac{B(x, y, 0) - B(0, 0, 0)}{B(0, 0, 0)} \right|$$

3. Use unique results \mathbf{x}_1 from stage 1 as starting points for the stage 2 optimization.
4. **Stage 2 optimization.** Minimize \mathbf{x} (subject to respective geometry constraints) with the objective function:

$$C_2(\mathbf{x}) = \Delta_B \cdot \bar{\eta}_{ROI}$$

As before, $\Delta_B = |B(0, 0, 0) - 10|$, the L1 norm of the magnetic field magnitude at the ROI center (in Gauss) relative to the target 10G.

5. Record the results \mathbf{x}_2 as the final optimized geometry parameters.

For Stage 1 and 2, we use the direct search Nelder-Mead simplex algorithm with adaptive parameters for objective function minimization, which has been shown to provide an advantage for optimizing high-dimensional problems [36] over the standard Nelder-Mead algorithm [37].

The Nelder-Mead algorithm in stage 1 uses a convergence threshold of 10^{-12} . The maximum number of iterations for each shot is 5×10^3 . In stage 2, the convergence threshold is 10^{-18} , and the maximum number of iterations for each shot is 5×10^3 . The Nelder-Mead optimizer terminates when either successive objective function evaluations become smaller than the convergence threshold, or the maximum number of iterations is reached.

2.4.2 Single-stage optimization scheme, a.k.a. *Samwise*

In addition to *Pippin*, we devise a single-stage optimization scheme, named *Samwise*²:

1. As before, generate n_{shots} random shots of starting parameter guesses for a chosen geometry. Each initial guess is a vector \mathbf{x}_0 with the i th element $x_{0,i}$ randomly drawn from the uniform distribution $U(a_i, b_i)$, where a_i and b_i are the minimum and maximum constraints imposed on the i th dimensional parameter.
2. **Single-stage optimization.** Minimize \mathbf{x} (subject to geometry constraints) with the piecewise objective function:

$$\begin{aligned} C(\mathbf{x}) &= \left| \frac{B(0, 0, 0) - 10}{10} \right| && \text{if } |B(0, 0, 0) - 10| > 0.1 \\ &= \bar{\eta}_{ROI} && \text{if } |B(0, 0, 0) - 10| < 0.1 \end{aligned}$$

As before, $\bar{\eta}_{ROI} = \frac{1}{101^2} \sum_{x=1}^{101} \sum_{y=1}^{101} \left| \frac{B(x, y, 0) - B(0, 0, 0)}{B(0, 0, 0)} \right|$ using the discretization of the 101×101 grid points on the $20\text{mm} \times 20\text{mm}$ ROI.

3. Record the results \mathbf{x}_f as the final optimized geometry parameters.

²Named after another hobbit from the Lord of the Rings. This one because there are plenty of magnetic rings being optimized, and it uses a *piecewise* function. Hence, *Samwise*.

The same Python packages are used as in *Pippin*. The convergence threshold is 10^{-18} , and the maximum number of iterations for each shot is 5×10^3 .

2.5 Candidate geometry selection

Candidate geometries are defined as permanent magnet structures generating a central field strength within $\pm 1\%$ of the target ($|B_0| = 10\text{G}$), and average nonuniformity $\bar{\eta}_{ROI} = 10^{-7}$ (0.1ppm) or better. Candidate geometries are then ranked in order of lowest to highest $\bar{\eta}_{ROI}$, with the lowest $\bar{\eta}_{ROI}$ geometry being the best candidate. These geometries are used to seed parameters for further simulations, possibly through finite-element models, and for eventual manufacturing.

2.6 Computation and parameters

2.6.1 Optimization scheme parameters

In each N-ring geometry optimization, $n_{shots} = 50$, and for each rod mangle optimization run with a specific number of rods, $n_{shots} = 25$.

2.6.2 Materials

The material properties of high-grade SmCo with $B_{rem} = 1.09\text{T}$ are used in the following simulations, aligning with B_{rem} values for the 30H to 32H grades of SmCo offered by Stanford Magnets [38]. While the material response of high-grade SmCo is typically $\mu_r \approx 1.05$, it is approximated to $\mu_r = 1$ for the simulation. SmCo is also the permanent magnet material of choice for cryogenic environments, with a temperature dependence of $-0.04\%/\text{K}$ [39], among the lowest of any material [12].

2.6.3 Computation

We perform these simulations in Python, using the Magpylib package for magnetic simulations, Numpy and Scipy packages for numerical optimization, and Plotly and Matplotlib packages for data visualization.

The Magpylib Python package enables robust and efficient magnetic simulations using vectorized analytical approximations [40], and was chosen to facilitate rapid development of the optimization schemes. The approximations return high-quality results for hard magnetic materials despite not presently supporting material demagnetization responses, with field strength errors $< 1\%$ for materials of $\mu_r < 1.05$ [41]. Also, the error decreases with increasing distance from the magnetized material [Ibid.], and so in the simulations that follow, it is anticipated to be less prevalent considering the centrally-located ROI that sits at a distance from magnetized material. The inherent symmetries in the chosen geometries may also further mitigate the impact of neglecting material response on net field strength inhomogeneity over the ROI.

Optimizations and simulations in Python were performed on a 2020 M1 MacBook Pro with 16GB RAM.

3 Nominal Helmholtz coil performance benchmark

The Helmholtz coil is analyzed within our Magpylib-based framework to provide a nominal performance benchmark for the optimized permanent magnet structures. Helmholtz coils are an electromagnetic two-coil system commonly used to generate uniform magnetic fields for sensor calibration, MRI, among other uses [42]. This makes it a suitable yardstick against which the optimized PMC performance can be measured.

The on-axis field strength at the midpoint of the Helmholtz coil system is derived from the Biot-Savart Law, and is given by:

$$B_0 = \left(\frac{4}{5}\right)^{\frac{3}{2}} \frac{\mu_0 N I}{a}$$

where a is the coil radius, which is also the separation distance of the two coils, I is the current carried by each coil in Amperes, and N is number of turns in each coil [16]. The area with field strength nonuniformity < 0.1 ppm between the coils scales as a increases.

At $B_0 = 10\text{G} = 10^{-3}\text{T}$ and setting the coil radius to the maximum allowed value $a = 170\text{mm}$, 189.0619 Ampere-turns per coil is needed to generate this field, potentially contributing to substantial Ohmic heating.

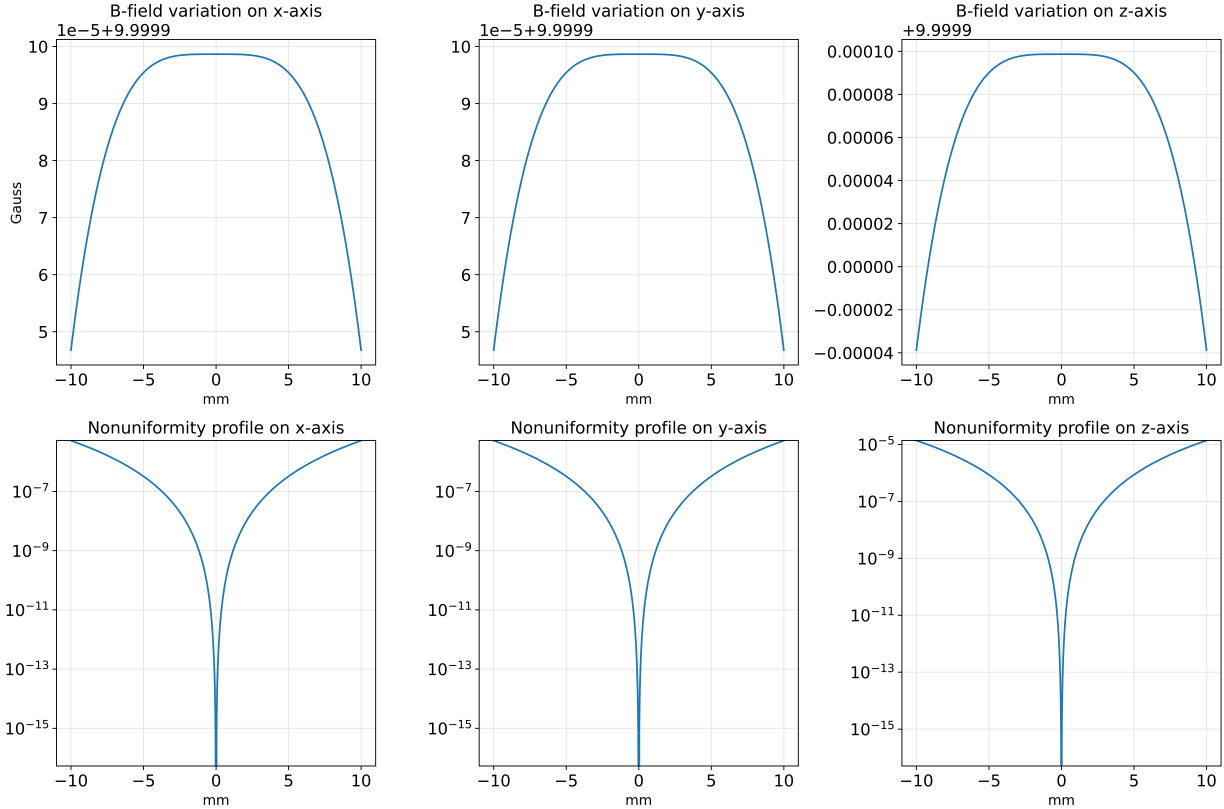


Figure 4: Central field strength and nonuniformity profiles for the Helmholtz coil along the x , y , and z axes.

Simulating this coil system gives the magnetic field strength and nonuniformity profiles found in Figure 4. The average nonuniformity over the ROI is $\bar{\eta}_{ROI} = 3.3600 \times 10^{-6}$, which fails to qualify the Helmholtz coil as a candidate geometry.

4 Results for magnetic field optimization

The results for geometries optimized through the Pippin and Samwise schemes are discussed here. It is noted that for certain structures, there is convergence to both +10G and -10G following the proposed optimization schemes. Positive field strength values represent the net field at the center of the ROI pointing parallel to the $+z$ direction of magnetization, and negative values represent an antiparallel field direction. For integration into trapped-ion hardware, permanent magnets producing either field strength directions can be utilized.

4.1 2 ring geometry

4.1.1 *Pippin* scheme

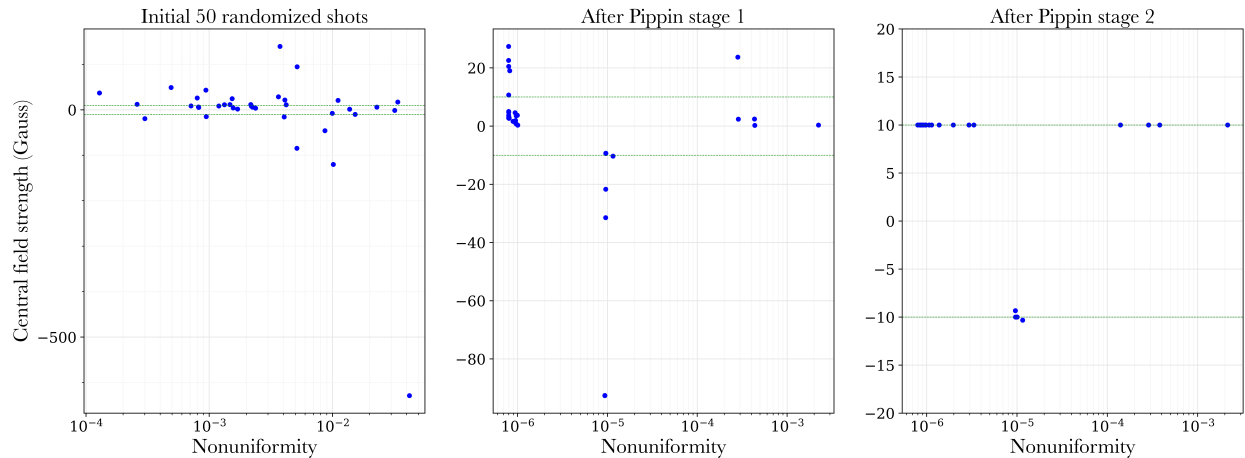


Figure 5: B_0 and $\bar{\eta}_{ROI}$ for 2 ring geometries through each stage of the *Pippin* optimization scheme. Each point denotes the performance of a single parameter set corresponding to a geometry. $\pm 10\text{G}$ field strengths shown by the horizontal green lines. 50 shots converged to 38 unique parameter sets after Pippin stage 1. Of these, 32 parameter sets demonstrated convergence to within $\pm 1\%$ of $|B_0| = 10\text{G}$ after Pippin stage 2. Although significant improvement in nonuniformity was observed, none of the final parameter sets achieved the 0.1ppm threshold, and no candidate geometries were identified.

4.1.2 Samwise scheme

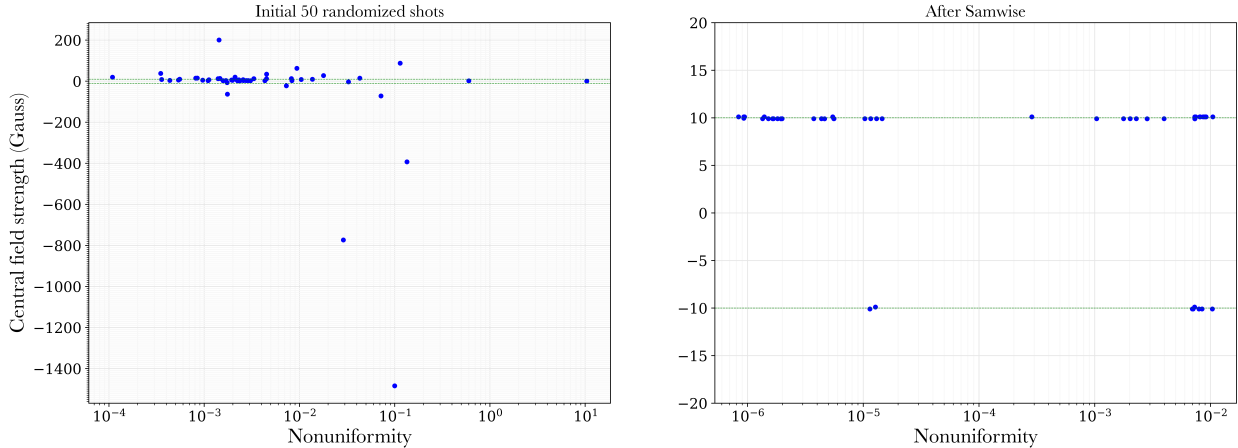


Figure 6: B_0 and $\bar{\eta}_{ROI}$ for 2 ring geometries before and after the *Samwise* optimization scheme. Each point denotes the performance of a single parameter set corresponding to a geometry. $\pm 10\text{G}$ field strengths shown by the horizontal green lines. All 50 shots converged to unique parameter sets after Samwise. Of these, 46 parameter sets converged to within $\pm 1\%$ of $|B_0| = 10\text{G}$, with the remaining 4 within $\pm 1.0001\%$ of the target value. Although significant improvement in nonuniformity was observed, none of the final parameter sets achieved the 0.1ppm threshold, and thus, no candidate geometries were identified.

4.2 3 ring geometry

4.2.1 Pippin scheme

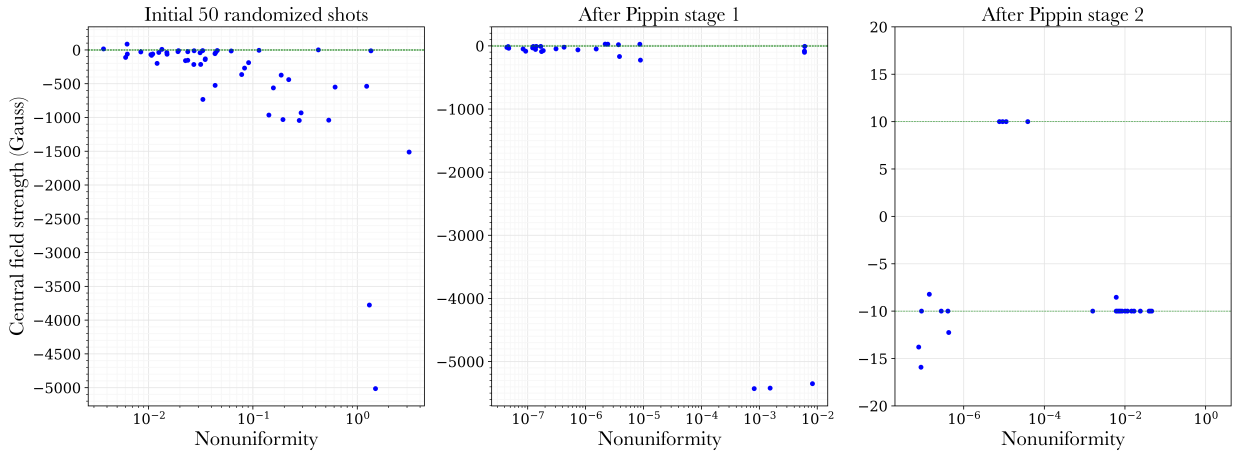


Figure 7: B_0 and $\bar{\eta}_{ROI}$ for 3 ring geometries through each stage of the *Pippin* optimization scheme. $\pm 10\text{G}$ field strengths shown by the horizontal green lines. The spread of magnetic field strengths after stage 2 is truncated to a range within $\pm 20\text{G}$ for clarity. No candidate geometries were identified.

4.2.2 Samwise scheme

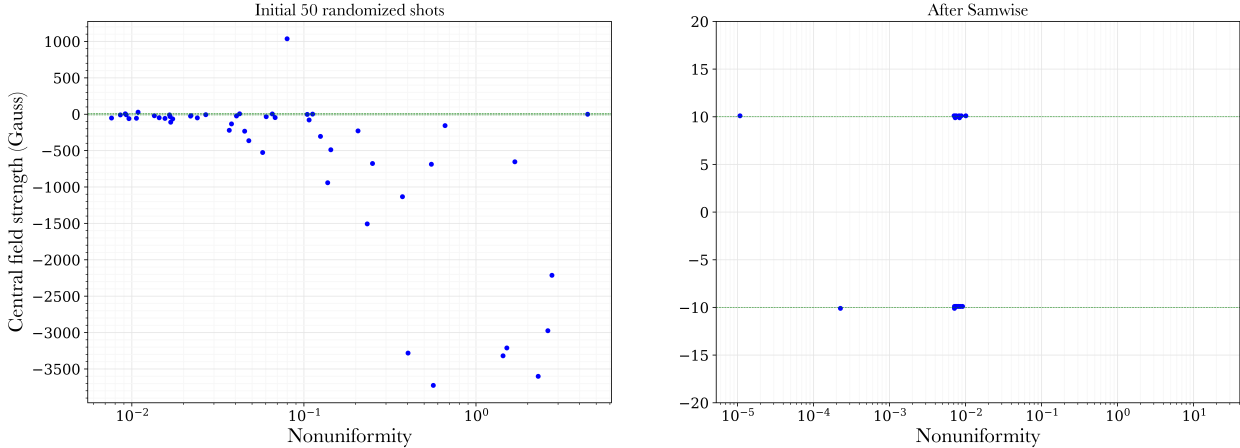


Figure 8: B_0 and $\bar{\eta}_{ROI}$ for 3 ring geometries before and after the *Samwise* optimization scheme. ± 10 G field strengths shown by the horizontal green lines. The spread of final magnetic field strengths is truncated to a range within ± 20 G for clarity. No candidate geometries were identified from this process.

4.3 4 ring geometry

4.3.1 Pippin scheme

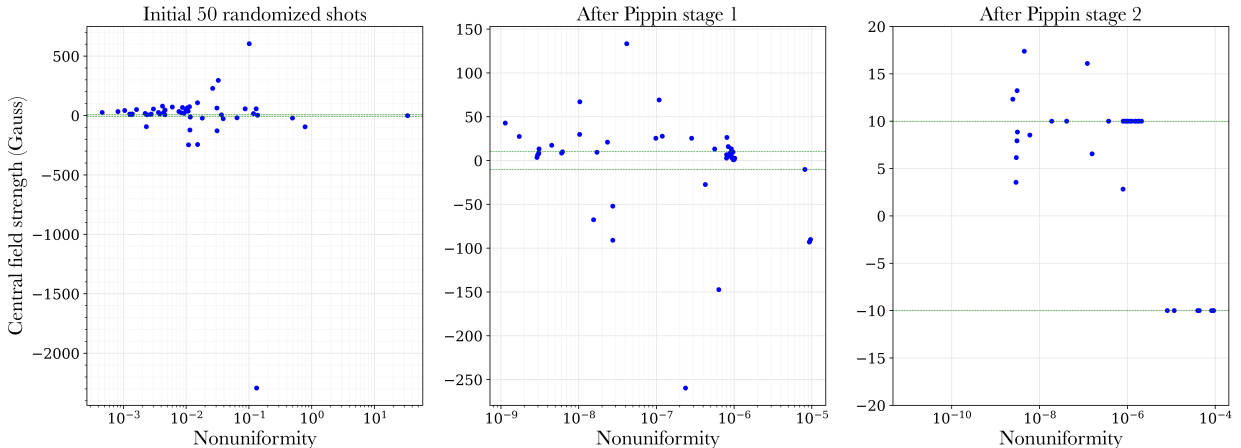


Figure 9: B_0 and $\bar{\eta}_{ROI}$ for 4 ring geometries through each stage of the *Pippin* optimization scheme. ± 10 G field strengths shown by the horizontal green lines. The spread of magnetic field strengths after stage 2 is truncated to within ± 20 G for clarity. 24 of 50 shots converged to within $\pm 1\%$ of $B_0 = 10$ G. From this, no candidate geometries were identified. The best-performing geometry from this scheme achieves $\bar{\eta}_{ROI} = 1.8995 \times 10^{-7}$ at $B_0 = 10.0000$ G.

4.3.2 Samwise scheme

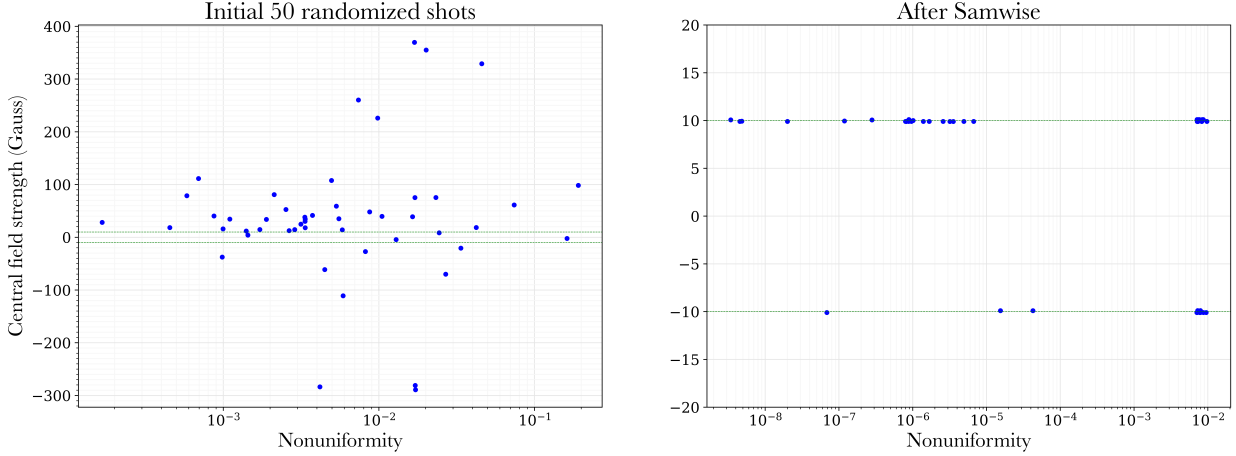


Figure 10: B_0 and $\bar{\eta}_{ROI}$ for 4 ring geometries before and after the *Samwise* optimization scheme. ± 10 G field strengths shown by the horizontal green lines. The spread of final magnetic field strengths is truncated to within ± 20 G for clarity. 37 of 50 shots converged to within $\pm 1\%$ of $|B_0| = 10$ G, and all 50 converged to within $\pm 1.0001\%$ of $|B_0| = 10$ G. Of these 50 geometries, 5 candidate geometries are identified. The best-performing candidate geometry achieves $\bar{\eta}_{ROI} = 3.4147 \times 10^{-9}$ at $B_0 = 10.066$ G.

4.4 Overall N-rings comparisons

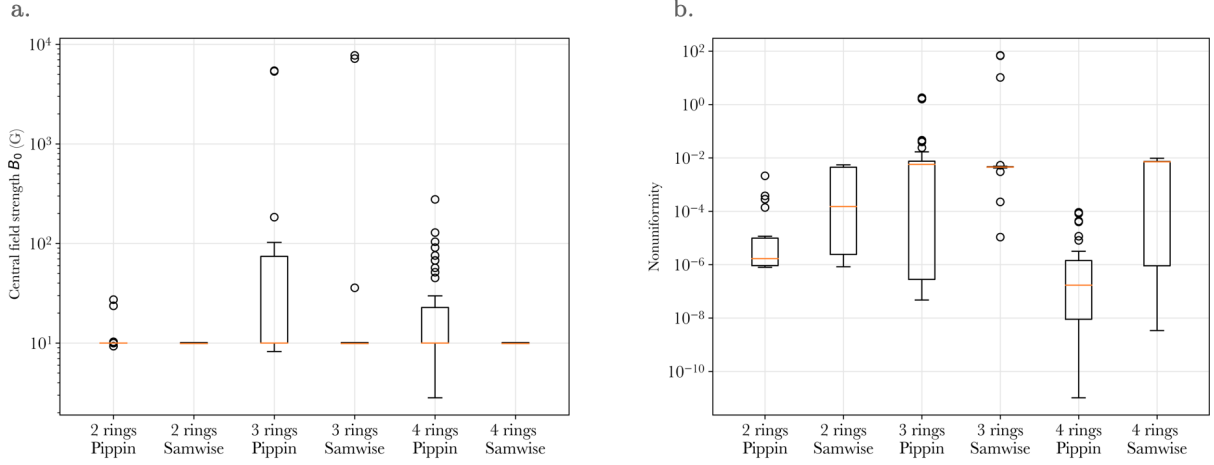


Figure 11: **a.** The Samwise scheme provides much better convergence to the target field strength $B_0 = 10$ G than the Pippin scheme given the significantly smaller spread in results. **b.** The Pippin scheme appears to have an advantage in retaining low nonuniformity during optimization, resulting in both lower median and minimum $\bar{\eta}_{ROI}$ than the Samwise scheme across all N-ring configurations tested.

4.5 Best N-rings candidate geometry analysis

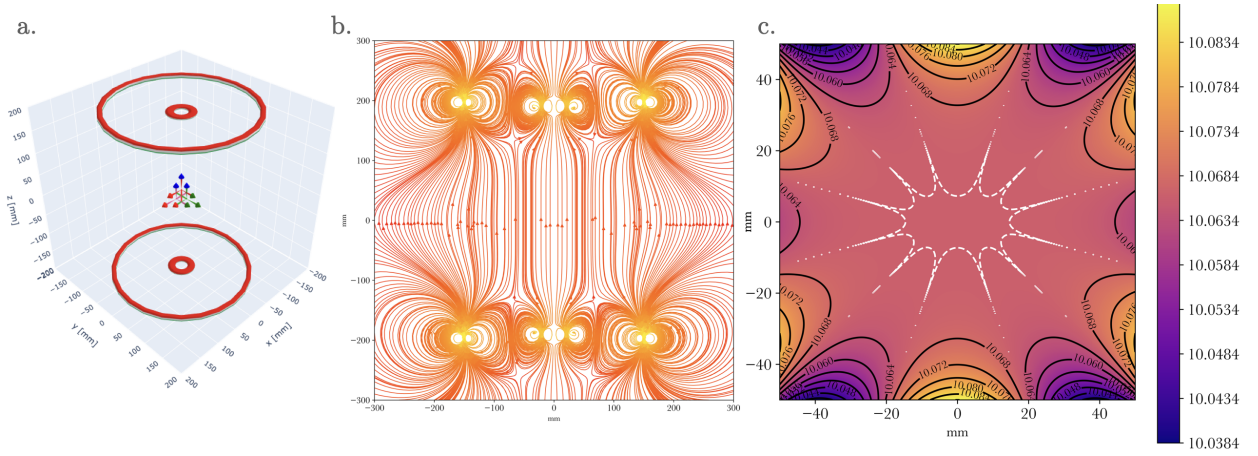


Figure 12: **a.** 3D representation of the best candidate 4-ring structure, obtained through the *Samwise* optimization scheme. **b.** Spatial distribution of magnetic flux in the xz -plane due to this 4-ring structure, noting that in the $z = 0$ plane there are no x or y components of the magnetic field. **c.** Spatial distribution of magnetic field strength in the xz -plane, along with a white-dashed outline of the central region with $< 10^{-7}$.

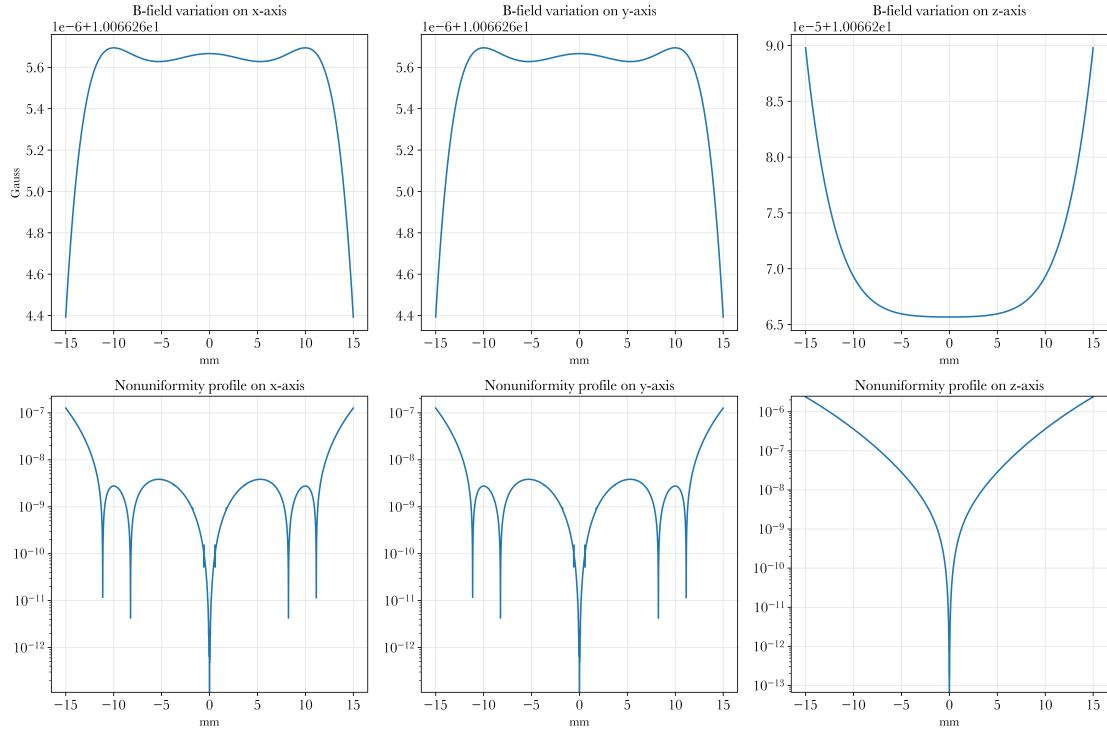


Figure 13: B_0 and nonuniformity profiles for the best N-rings geometry along coordinate axes.

The best N-rings candidate geometry is a 4-ring structure obtained through the *Samwise* scheme, giving $\bar{\eta}_{ROI} = 3.4147 \times 10^{-9}$ and $B_0 = 10.066\text{G}$. For this geometry, ringset 1 parameters are: $r_1 = 13.9338\text{mm}$, $w_1 = 16.0981\text{mm}$, $t_1 = 2.4895\text{mm}$, $d_1 = 190.7487\text{mm}$. Ringset 2 parameters are: $r_2 = 146.0266\text{mm}$, $w_2 = 9.9622\text{mm}$, $t_2 = 7.7810\text{mm}$, $d_2 = 197.0063\text{mm}$.

Over the ROI, the magnetic field nonuniformity remains below 10^{-8} . The maximal planar extent in $z = 0$ with nonuniformity $< 10^{-7}$ is a disc of diameter 28mm (see Figure 20).

The effective coverage ratio (ECR) for a given structure is defined as the ratio of homogenous volume, V_η , to the volume of the minimum bounding cuboid that can contain the permanent magnet configuration, V_β (metric adapted from [17]). For this 4-ring geometry:

$$V_\beta = (2d_2 + t_2) \times (2w_2 + 2r_2)^2 = 3.9107 \times 10^7 \text{mm}^3$$

and V_η is a volume containing the ROI with nonuniformity $< 10^{-7}$ over its entire extent (see Figure 12c). It is computed by discretizing a central region measuring 50mm \times 50mm \times 50mm into $101 \times 101 \times 101$ identical voxels, and computing the point nonuniformity in the center of each cube. This allows us to construct the 3D uniform region to a voxel resolution of $\left(\frac{50}{101}\right)^3 = 0.1213\text{mm}^3$. Given this:

$$\text{ECR} = \frac{V_\eta}{V_\beta} = \frac{1.1918 \times 10^5 \text{mm}^3}{3.9107 \times 10^7 \text{mm}^3} \times 100\% = 0.0305\%$$

4.6 Discussion of N-ring geometry optimization schemes

We have presented two efficient schemes for rapidly optimizing permanent magnet geometries for target field strengths and nonuniformity. These schemes, named Pippin and Samwise, offer different advantages for the multiobjective optimization problem we have described. Pippin is well-suited to maintaining low nonuniformity levels in resultant geometries, at the expense of convergence to the target magnetic field strength. Taken together, this leads to a lower yield of geometries that satisfy both criteria. Therefore, the Pippin scheme would be recommended for applications where low nonuniformity is of paramount importance, and where variance may be tolerated in the field strength. Conversely, the Samwise scheme excels at converging to both criteria, and provides exceptional yield for geometries meeting the target field strength: well over 70% of 2, 3, 4-rings results achieved the target field strength. However, this comes at the expense of the degree of nonuniformity attained, and it must also be noted that Samwise falls short on 3-ring geometries relative to Pippin. We hypothesize that this behavior may be generalized to odd-numbered N-ring geometries, and this is an area for further study.

We have also identified several candidate geometries provided by these optimization schemes, and analyzed the best candidate: a 4-ring configuration attaining $\bar{\eta}_{ROI} = 3.4147 \times 10^{-9}$ at $B_0 = 10.067\text{G}$. This candidate geometry provides a starting point for further finite-element analysis and optimization.

The performance of the optimized structures further suggest that the minimum field strength nonuniformity achieved decreases as a function of N rings, and imply that a lower bound

exists for the nonuniformity attainable for each N . This would present an opportunity to further control field strength nonuniformity by introducing more ringsets. However, working with higher orders of N also comes at the tradeoff of easily manufacturing such permanent magnets, and may introduce greater variances and errors in alignment.

4.7 Rod mangle (Halbach cylinder) geometry

The rod mangle structure was also investigated and optimized using the Pippin and Samwise schemes.

4.7.1 *Pippin* scheme

The Samwise scheme was used to optimize rod mangle geometries with $6 \leq N \leq 16$. For each N , 25 shots are used to optimize the geometry. Stage 1 results of the Pippin scheme are used to determine if lower bounds exist for the average nonuniformity over ROI for each number of rods N .

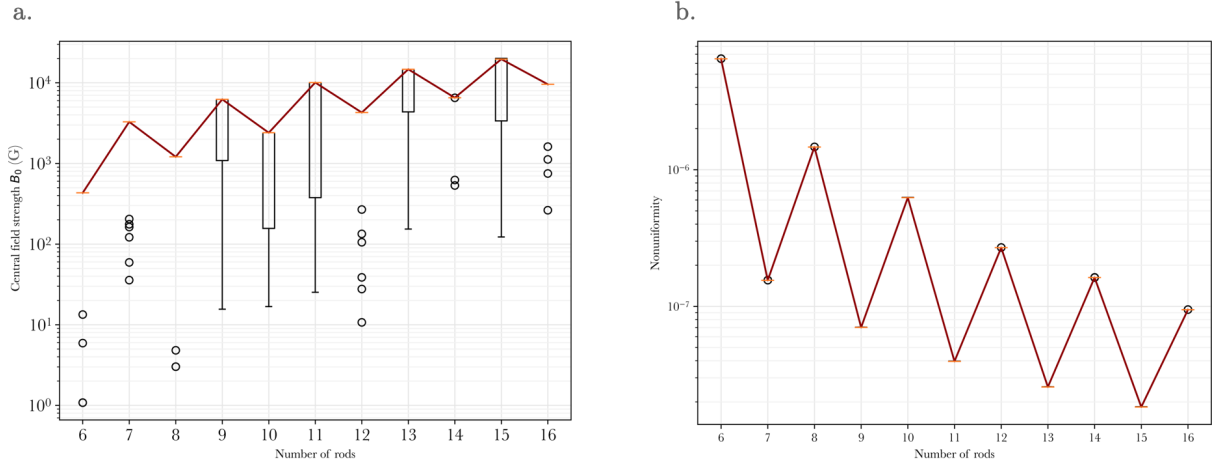


Figure 14: **Pippin stage 1** outputs for N -rod mangles with plotted medians. **a.** The median central magnetic field strength appears to have a dependence on the parity of the number of rods, such that for each odd N , the median B_0 is higher than that of both adjacent $N-1$ and $N+1$ geometries with even numbers of rods over the range of N tested. **b.** Similarly, the median $\bar{\eta}_{ROI}$ appears to be tied to the parity of the number of rods. Each odd N configuration has a lower median average nonuniformity than both $N-1$ and $N+1$ geometries over the range of N tested.

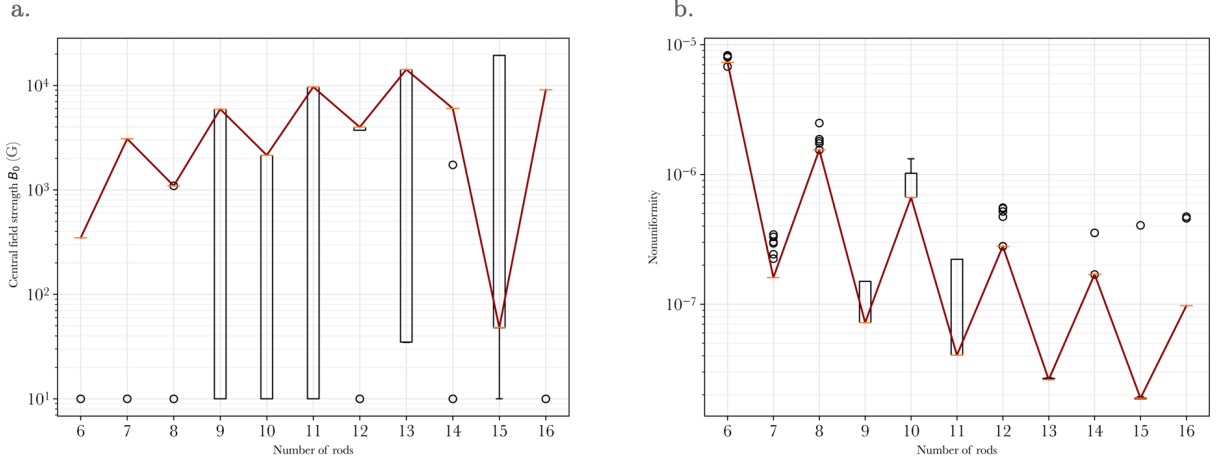


Figure 15: **Pippin stage 2** outputs for N-rod mangles with plotted medians. **a.** The dependence of the median B_0 on the parity of N still generally features prominently except for $N = 15$. However, the spread of B_0 increases significantly following stage 2, and this is primarily due to a proportion of geometries successfully converging to the target B_0 , with others failing to do so and staying near their initial field strength values. **b.** Similarly, the dependence of average nonuniformity $\bar{\eta}_{ROI}$ on parity of N is reflected here as well. The spread of $\bar{\eta}_{ROI}$ increases from stage 1, as geometries that converge towards the target of $B_0 = 10\text{G}$ tend to have higher $\bar{\eta}_{ROI}$.

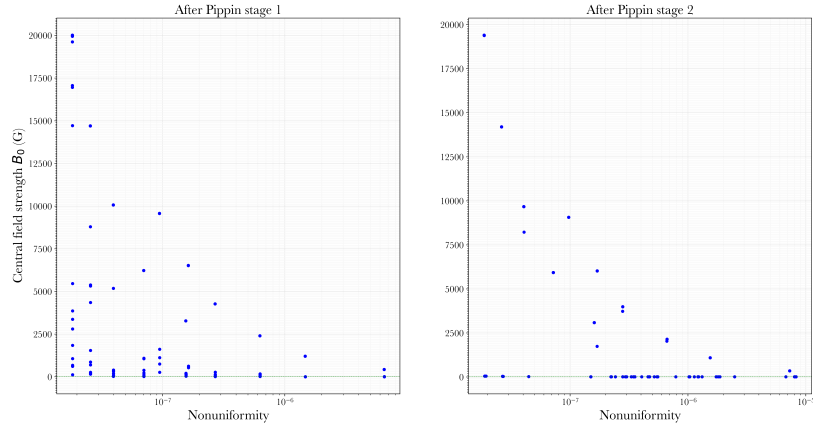


Figure 16: B_0 against $\bar{\eta}_{ROI}$ of optimized rod mangle geometries across all N rods ($6 \leq N \leq 16$). The Pippin scheme enables a number of geometries to converge to average nonuniformity $< 0.1\text{ppm}$ following stage 1. However, after stage 2, convergence to target field strength typically comes at expense of the average nonuniformity. Indeed, there are no candidate geometries concurrently satisfying $\bar{\eta}_{ROI} \leq 10^{-7}$ and $B_0 = 10\text{G}$ from the Pippin optimization scheme.

Although no candidate geometries were returned via the Pippin optimization scheme, the best rod mangle (Halbach cylinder) configuration with lowest $\bar{\eta}_{ROI}$ and central field strength

within $\pm 1\%$ of 10G was a 9-rod structure achieving $\bar{\eta}_{ROI} = 1.4990 \times 10^{-7}$ at $B_0 = 10$ G. The parameters for this geometry are $d_{cyl} = 1$ mm, $h_{cyl} = 640$ mm, $D = 70.0339$ mm. This is particularly surprising as it was expected that a larger number of rods would more closely approximate the ideal Halbach cylinder, and therefore achieve a lower $\bar{\eta}_{ROI}$ at the target field strength.

The thin ($d_{cyl} = 1$ mm) and extended rods ($h_{cyl} = 640$ mm) required to produce this geometry may prove challenging to manufacture in practice, since SmCo is known to be brittle and may not provide sufficient structural integrity to form the rod as a single contiguous piece. Further discussion on manufacturing tolerances is covered in a subsequent section.

4.7.2 Samwise scheme

The Samwise scheme was used to optimize rod mangle geometries with $6 \leq N \leq 12$.

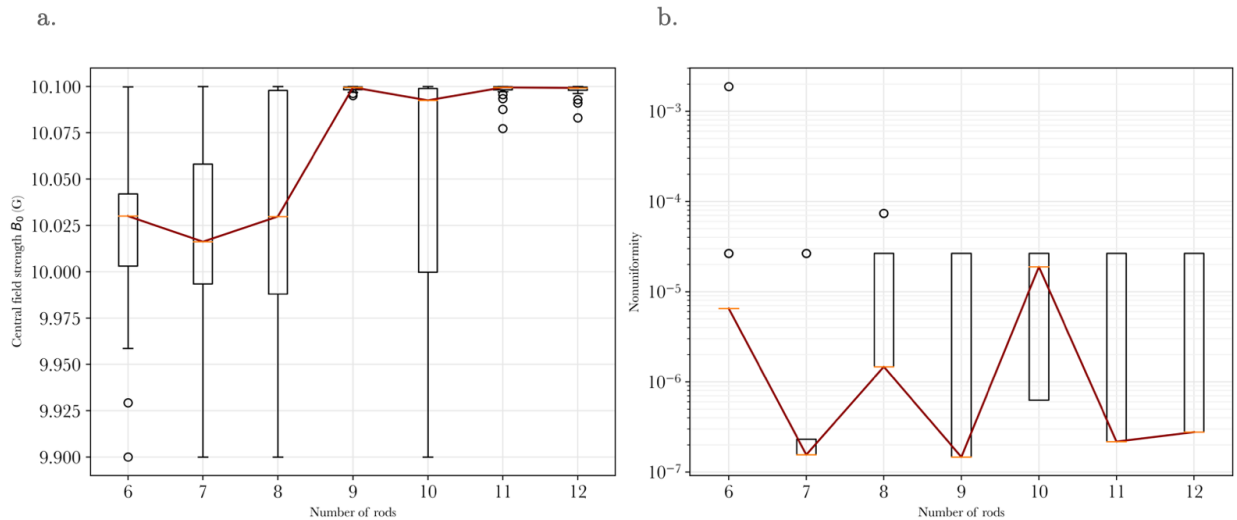


Figure 17: **a.** The Samwise scheme provides excellent convergence to the target field strength, and almost all results lie within the range $\pm 1\%$ of $B_0 = 10$ G. **b.** $\bar{\eta}_{ROI}$ performance is on par with that from the Pippin scheme.

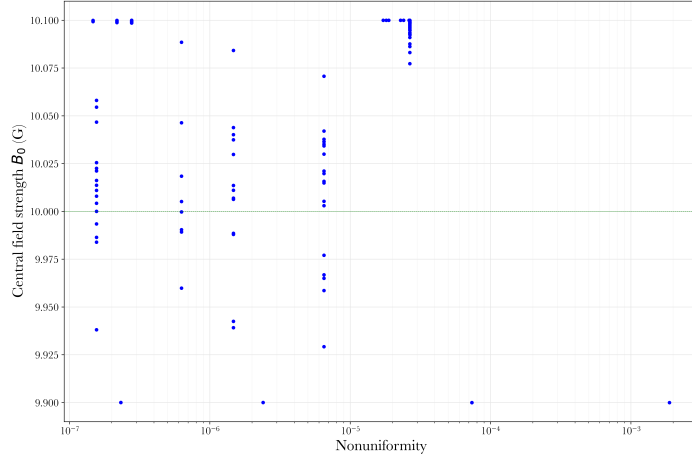


Figure 18: B_0 against $\bar{\eta}_{ROI}$ of rod mangle geometries across all N rods ($6 \leq N \leq 12$), optimized through the Samwise scheme.

4.8 Discussion of rod mangle geometry optimization schemes

Given the exceptional performance of the Samwise scheme in convergence to the target B_0 (close to 100% yield within the $\pm 1\%$ range) and a significant yield of low $\bar{\eta}_{ROI}$ geometries, the Samwise scheme is preferred to the Pippin scheme for multiobjective optimization of rod mangle geometries.

A caveat is that the Samwise scheme could be more computationally expensive in certain cases than the Pippin scheme to implement, as a complete Samwise optimization for each $N = 11, 12$ was completed in about 4-6h on the experimental hardware, while that for Pippin was completed in 3-5h.

4.9 Best rod mangle geometry analysis

Both Samwise and Pippin schemes did not return candidate geometries, as all final values of $\bar{\eta}_{ROI}$ were greater than 0.1ppm. The best-performing geometry was obtained through the Samwise scheme, and has parameters $N = 9$, $d_{cyl} = 1\text{mm}$, $h_{cyl} = 640\text{mm}$, $D = 69.6867\text{mm}$. It achieves $\bar{\eta}_{ROI} = 1.4697 \times 10^{-7}$ and $B_0 = 10.0999\text{G}$.

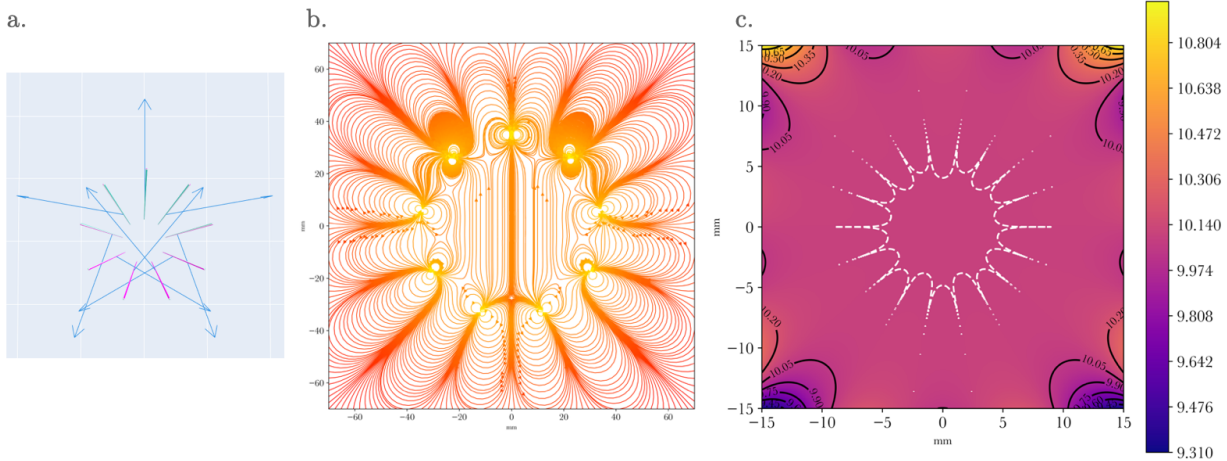


Figure 19: **a.** 3D representation of the best rod mangle geometry, obtained through the Samwise optimization scheme. The arrows depict the magnetization direction of each of the 9 rods. **b.** Spatial distribution of magnetic flux in the xz -plane due to this rod mangle geometry. **c.** Spatial distribution of magnetic field strength in the xz -plane, along with a white-dashed outline of the central region with $< 10^{-7}$.

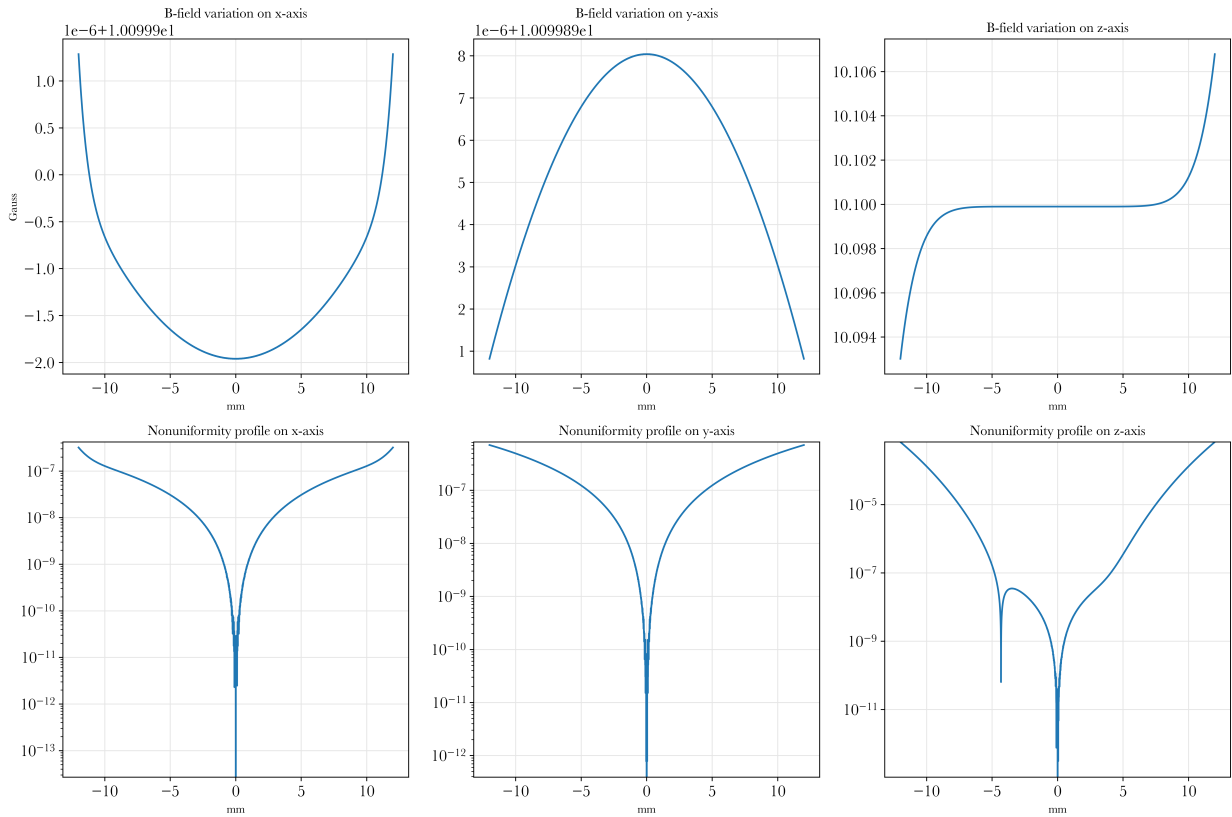


Figure 20: B_0 and point nonuniformity profiles for the best rod mangle geometry along the x , y , and z axes. The nonuniformity profile is best along the extended y -axis.

5 Permanent magnets in practice

The permanent magnet geometries simulated up to this point are ideal and absent of misalignments, demagnetization, and process variations. In practice, these physical sources of error often introduce variances in the nonuniformity and central field strength.

5.1 Manufacturing variations & constraints

One significant source of error arises from permanent magnet manufacturing tolerances. Tolerances refer to the allowable deviation of the manufactured product from the nominal dimensions of the design [43], and shrinks with increasing manufacturing precision. In terms of permanent magnets, manufacturing tolerances may result in the deposition of excess or insufficient magnetized material over the extent of the geometry, leading to spatial variations in the magnetic field strength supplied by the permanent magnet geometry. These deviations can lead to an increase in the average nonuniformity over the ROI, $\bar{\eta}_{ROI}$, and a deviation from the target central field strength $B_0 = 10\text{G}$.

The effect of these tolerances has been previously studied in the context of electric motors [44,45] as deviations generally result in the production of undesirable ‘cogging torque’ that compromises the efficiency and efficacy of these devices [46].

Here, we present a brief overview of the expected tolerances for permanent magnets placed in the context of trapped-ion applications, and conduct a brief survey of tolerance effects on $\bar{\eta}_{ROI}$ and B_0 .

The two most relevant permanent magnet materials used with trapped-ion devices are samarium cobalt (SmCo) and neodymium iron boron (NdFeB). The tolerances for both materials are relatively similar, and generally vary with the magnet grade, the fabrication process used, and the overall magnet size. For most manufacturers, the manufacturing tolerance for these ferromagnetic materials range from $\pm 0.05\text{mm}$ up to around $\pm 0.3\text{mm}$ [47–49] (Stanford Magnets, personal communication, July 27, 2023).

Manufacturing constraints also pose limits on the minimum dimensions of the permanent magnet. In particular, SmCo magnets chip and crack easily [48] and designs therefore require sufficient thickness to maintain structural integrity. The minimum thickness varies by manufacturing process and equipment used (Stanford Magnets, personal communication, July 27, 2023), and may be specific to each product manufacturer. To prevent cracking during setup, dedicated support structures may be designed to accommodate and secure the SmCo permanent magnets within the cryogenic chambers used in trapped-ion quantum hardware.

5.2 Magnetization variations

Deviations in the remanence magnetization B_{rem} is another source of error in permanent magnets. This is generally dependent on the grade of magnet used, and typically varies between $\pm 0.01\text{T}$ to $\pm 0.03\text{T}$ for SmCo (2-17 ratio) and NdFeB [50,51] (and Stanford Magnets, personal communication, November 30, 2022).

The direction of magnetization is also subject to variation up to 4° from the specified magnetization axis [49].

Since the efficacies of permanent magnet geometries studied here (N-rings, rod mangle) have a strong dependence on magnetization direction and remanence, the presence of deviations in B_r and its axis can result in significant adverse effects in both the expected nonuniformity and central field strength (see Figure 22).

5.3 Nonidealized simulations

Simulations were conducted to analyze the performance of the rod mangle structure under variations. The nominal structure ($N = 9$, $d_{cyl} = 1\text{mm}$, $h_{cyl} = 640\text{mm}$, $D = 69.6867\text{mm}$) used here corresponds to the best-performing 9-rod mangle found using the Samwise scheme that achieves $\bar{\eta}_{ROI} = 1.4697 \times 10^{-7}$ and $B_0 = 10.0999\text{G}$.

5.3.1 Rod mangle dependence on rod height

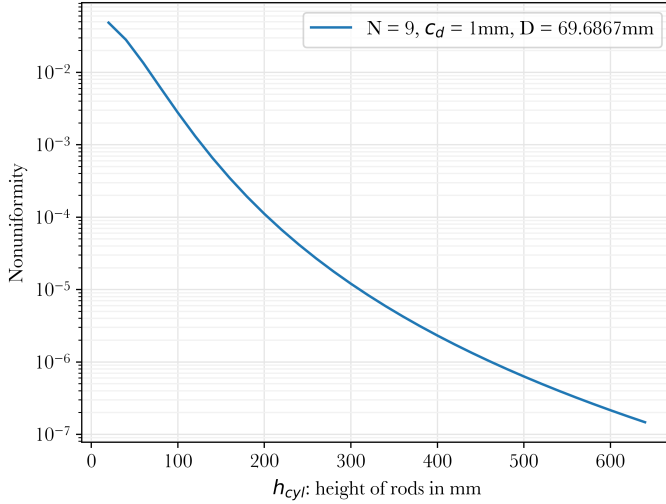


Figure 21: $\bar{\eta}_{ROI}$ decreases rapidly with increasing rod height. The ideal Halbach cylinder is infinitely long - a useful rod mangle will require an adequately long rod height to achieve low average nonuniformity in practice.

5.3.2 Rod mangle performance with manufacturing variations

The errors are defined as follows

$$\begin{aligned}\delta B_{rem} &\sim N(0, (\alpha \cdot 0.02)^2) \text{ in T} \\ \delta p_{deg} &\sim N(0, (\alpha \cdot 2)^2) \text{ in } {}^\circ \\ \delta r_{deg} &\sim N(0, (\alpha \cdot 2)^2) \text{ in } {}^\circ\end{aligned}$$

where δB_{rem} is the deviation from the nominal magnetization for a single rod, δp_{deg} is the angular displacement of a rod along the perimeter of the cylinder, δr_{deg} is the angular

displacement of the rod from its nominal rotation about its own axis, $\alpha \in [0, 2]$ and is swept over the interval in linear steps. $n_{shots} = 20$ was used for each α value.

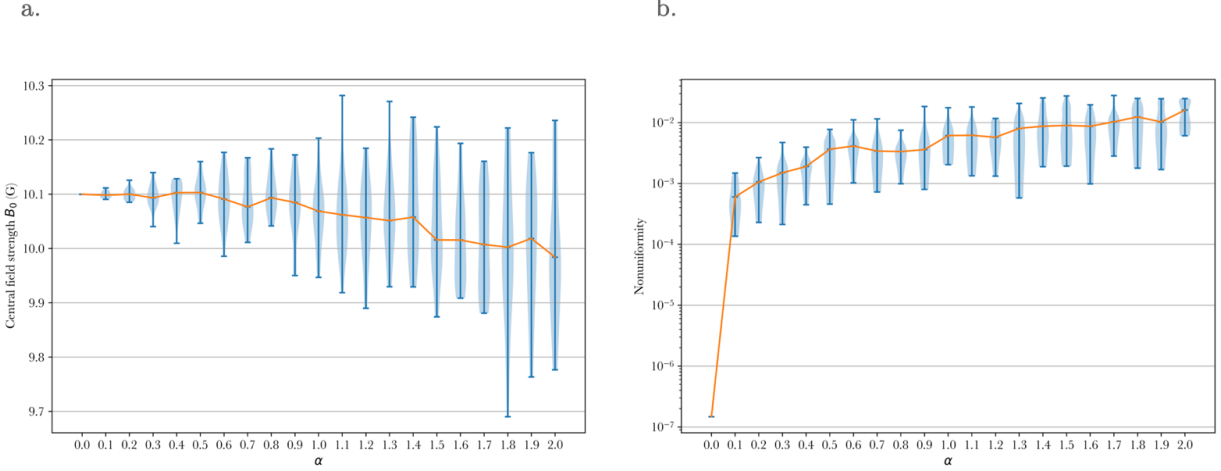


Figure 22: **a.** B_0 deviates from its nominal value as deviations increase in magnitude. **b.** A significant deviation for $\bar{\eta}_{ROI}$ is observed, and the median value generally increases for increasing α . At the same time, the spread of achieved B_0 values also generally increases. The violin plots also provide an overview of the distribution and skew of the data.

6 Design of fiber noise cancelation (FNC) system

6.1 Motivation for FNC

Trapped-ion quantum information processing requires the use of lasers with stable and narrow linewidth to enable sustained coherence times. Typically, light from a laser source is coupled into optical fibers for transmission to the ion trap setup. These extended optical fibers generally extend over a few meters in length, and may cross several rooms. However, the transmitted signal is highly-susceptible to perturbations, and can accumulate phase noise due to environmental fluctuations in temperature and pressure [23]. An active fiber noise cancelation system mitigates this source of error by writing a corrective phase on the transmitted signal, canceling out the accumulated phase noise transmitted to the experiment-facing end of the fiber.

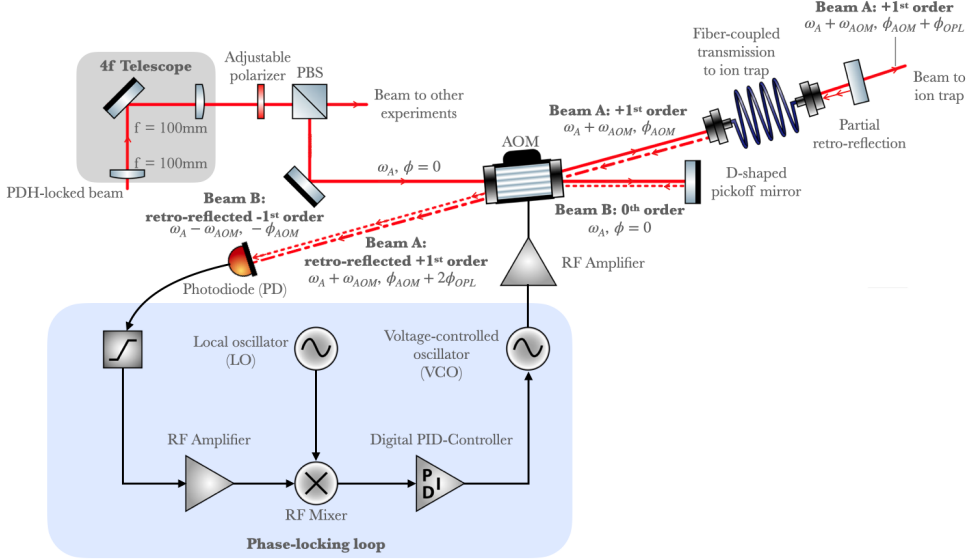


Figure 23: Setup of FNC system. Electrical connections are shown in black, while the 729nm beam path is shown in red. Dashed red lines indicate retro-reflections.

6.2 Theory

A scheme for fiber noise cancelation was first proposed by Ma et. al. [23] and leverages an error signal generated by heterodyning a stable-phase reference signal with the reflected signal from the experiment. A diagram of the full experimental setup is as shown in Figure 23.

The optical path length (OPL) traversed by a light wave in the absence of noise is given by

$$\text{OPL} = \int_C \mathbf{n}(\mathbf{s}) \cdot d\mathbf{s}$$

where C is the path traversed by the beam, and $\mathbf{n}(\mathbf{s})$ is the refractive index of the propagation medium at the point \mathbf{s} along the path [52]. Given the presence of environmental noise, the $\mathbf{n}(\mathbf{s})$ term becomes time-varying, and so the OPL acquires a time dependence. For a signal traversing through a fiber, it accrues a time-varying phase $\phi_{OPL}(t)$ upon emerging at the endpoint that fluctuates over the characteristic timescales of the environmental noise. The electric field at the end of the fiber therefore oscillates with the OPL phase [24]:

$$\mathbf{E} = E_0 \cos(\omega t + \phi_{OPL}(t))$$

To generate the heterodyne signal, we frequency modulate the outbound beam and the reference beam using an acousto-optic modulator (AOM) as shown in Figure 23.

The incoming laser signal entering the AOM has a frequency ω_A . The AOM modulates the $+1^{st}$ order diffracted beam by the acoustic frequency (emerging signal has frequency $\omega_A + \omega_{AOM}$) and imparts a phase determined by the acoustic signal ϕ_{AOM} . We denote this beam as ‘beam A’. The 0th order beam has no additional imparted phase or frequency modulation. We denote this beam as ‘beam B’.

Beam A is fiber-coupled and transmitted via a 15m optical fiber to the ion-trap experiment in an adjacent room. This beam accumulates a phase $\phi_{OPL}(t_1)$ at the experiment-end due to the OPL and environmental noise that couples into the fiber. Beam A is deliberately partially reflected back through the fiber via index contrasts at the fiber-end interface, and accrues phase $\phi_{OPL}(t_2)$ on the return transmission path. The time of flight (TOF) for beam A to complete one round-trip between the AOM to the experiment-end is given by:

$$\tau_{TOF} = \frac{2 \cdot \text{OPL}}{c} \approx \frac{2 \times 15\text{m}}{3 \times 10^8 \text{m} \cdot \text{s}^{-1}} = 0.1\mu\text{s}$$

and it is significantly shorter than the characteristic timescale τ_{noise} on which the environmental noise varies (environmental noise is taken to vary at 10kHz) [24]:

$$\tau_{TOF} \ll \tau_{noise}, \quad \tau_{noise} \approx \frac{1}{10\text{kHz}} = 100\mu\text{s}$$

Thus, over a single round-trip, the time-varying phase due to the OPL can be taken as constant, giving $\phi_{OPL}(t_1) = \phi_{OPL}(t_2) \equiv \phi_{OPL}$. The total accrued phase when beam A returns to the AOM is given by $\phi_{AOM} + 2\phi_{OPL}$. It is then sent through the AOM once more, and emerges undiffracted since it does not satisfy the Bragg angle.

Concurrently, beam B (the initial 0th order undiffracted beam) is retro-reflected through the AOM using a D-shaped pickoff mirror. This beam emerges from the AOM as the -1st diffracted order, with modulated frequency $\omega_A - \omega_{AOM}$ and phase $-\phi_{AOM}$.

Beams A and B are superposed with each other and collected on a photodiode (PD). In the time domain, the superposed electric field at the PD can be described as oscillating in the time domain as follows:

$$E_{PD} = E_A \exp(i(\omega_A + \omega_{AOM})t + \phi_{AOM} + 2\phi_{OPL}) + E_B \exp(i(\omega_A - \omega_{AOM})t - \phi_{AOM})$$

Taking the phase of beam B = 0 (shifting all phase terms to the term representing beam A), the intensity measured on the photodiode is then given by

$$\begin{aligned} I_{PD} &\propto |E_{PD}|^2 = E_{PD} \cdot E_{PD}^* \\ &= (E_A \exp(i((\omega_A + \omega_{AOM})t + 2\phi_{AOM} + 2\phi_{OPL})) + E_B \exp(i(\omega_A - \omega_{AOM})t)) \cdot \\ &\quad (E_A \exp(-i((\omega_A + \omega_{AOM})t + 2\phi_{AOM} + 2\phi_{OPL})) + E_B \exp(-i(\omega_A - \omega_{AOM})t)) \\ &= |E_A|^2 + |E_B|^2 + 2|E_A||E_B| \exp(i((2\omega_{AOM})t + 2\phi_{AOM} + 2\phi_{OPL})) + \\ &\quad 2|E_A||E_B| \exp(-i((2\omega_{AOM})t + 2\phi_{AOM} + 2\phi_{OPL})) \\ &= |E_A|^2 + |E_B|^2 + 2|E_A||E_B| \cos(2\omega_{AOM}t + 2\phi_{AOM} + 2\phi_{OPL}) \end{aligned}$$

and thus the intensity signal has a beat note at twice the acoustic frequency applied by the AOM ($2\omega_{AOM}$), carrying a net phase $2\phi_{AOM} + 2\phi_{OPL}$. Since the corresponding generated photocurrent is linearly proportional to the incident intensity, the photocurrent signal also varies at the same frequency as the beat note.

Using a low-pass filter to remove any of the higher frequency elements on this photocurrent signal, it is then mixed with the local oscillator (LO) signal using an RF mixer. The LO source

operates at frequency $2\omega_{AOM}$. The mixer output is then fed into a digital PID-controller, which uses the net phase offset between the intensity and LO signals as the error signal.

To minimize the error signal, the PID-controller output is used to adjust the AOM phase to satisfy the condition $\phi_{AOM} = -\phi_{OPL}$, which enables complete cancelation of net accrued phase at the experiment-end of the fiber.

6.3 Experimental setup

The FNC setup is primarily located on a single optical table, with fiber-coupled beam transmission to an adjacent experiment room, where the ion trap is housed.

The system is implemented with a 729nm Ti:Sa laser source, which is locked to a cavity using the Pound-Drever-Hall method [22]. A $4f$ telescope composed of two plano-convex lenses of $f = 100\text{mm}$ is used to collimate the PDH-locked beam entering the FNC setup, near the edge of the Rayleigh range of the beam. This ensures that the beam waist remains compact for optimal AOM diffraction efficiency.

Due to the small beam separation between the two beams, a single D-shaped pickoff mirror is used to retro-reflect the 0^{th} order beam B. The AOM used is rated for a Bragg angle of 8.2mr at 690nm with a corresponding beam separation of 16.4mr , and so by fixing the pickoff mirror at a distance of about 100mm from the AOM, it is able to reflect only beam B without affecting propagation of beam A. The AOM used is driven by a VCO operating at 100MHz , allowing an expected photocurrent beat note frequency of 200MHz from the photodiode.

A Stanford Research Systems SIM960 is chosen as the PID controller for the system. A custom-made power supply was constructed for this device using two Traco Power AC to DC converter units supplying $\pm 15\text{V}$ and $+5\text{V}$ respectively, each powered by the mains supply.

As the FNC setup is presently underway, the beam path shown in Figure 23 and the following bill of materials is accurate as of Aug 14, 2023 and may be subject to change.

6.4 Bill of materials

Category	Device	Quantity
Optics	Thorlabs CP33 Lens Mount	2
	Thorlabs LA1509-B $f = 100\text{mm}$ plano-convex lens	2
	Thorlabs Polaris Mirror Mount	2
	Thorlabs 1" Broadband Dielectric Mirror, $400\text{-}750\text{nm}$	2
	Thorlabs 1" D-shaped Pickoff Mirror	1
	Thorlabs 1/2" Polarizing Beamsplitter Cube, $620\text{-}1000\text{nm}$	1
	Thorlabs Pedestal Post, <i>assorted</i>	As required
	Thorlabs Optics Mount Spacer, <i>assorted</i>	As required
	Thorlabs Pedestal Post Clamp	As required
	Thorlabs FT030-Blue Optics Fiber 15m length	1
	Thorlabs CFC5A-B Collimator	1

Category	Device	Quantity
Electronics	Gooch & Housego AOM 3100-125, <i>center frequency 100MHz</i>	1
	Mini-circuits ZHL-3A-S+ Amplifier	1
	Mini-circuits ZLW-1 Mixer	1
	Mini-circuits ZOS-150+ VCO	1
	Mini-circuits ZFL-11AD+ Amplifier, <i>for photodiode</i>	1
	Mini-circuits SMA attenuators, <i>assorted</i>	As required
	Stanford Research Systems SIM960 PID Controller	1
	Traco Power TXLN 035-23M3 +/-15V AC to DC Converter	1
	Traco Power TXLN 035-105 +5V AC to DC Converter	1
	SMC Cables	As required

7 Acknowledgements

The author would like to thank Professor Karan Mehta for his comprehensive and insightful guidance and opportunity to work on this summer research project, colleagues in the Photonics and Quantum Electronics group at Cornell for their supportive and earnest discussions, and the Engineering Learning Initiatives and James Moore '62 EE sponsorship for enabling this research.

References

- [1] T. P. Harty, D. T. C. Allcock, C. J. Ballance, L. Guidoni, H. A. Janacek, N. M. Linke, D. N. Stacey, and D. M. Lucas, *High-Fidelity Preparation, Gates, Memory, and Readout of a Trapped-Ion Quantum Bit*, Physical Review Letters **113**, 220501 (2014).
- [2] P. Wang, C.-Y. Luan, M. Qiao, M. Um, J. Zhang, Y. Wang, X. Yuan, M. Gu, J. Zhang, and K. Kim, *Single Ion Qubit with Estimated Coherence Time Exceeding One Hour*, Nature Communications **12**, 233 (2021).
- [3] K. R. Brown, A. C. Wilson, Y. Colombe, C. Ospelkaus, A. M. Meier, E. Knill, D. Leibfried, and D. J. Wineland, *Single-Qubit-Gate Error Below 10^{-4} in a Trapped Ion*, Physical Review A **84**, 030303 (2011).
- [4] J. I. Cirac and P. Zoller, *Quantum Computations with Cold Trapped Ions*, Physical Review Letters **74**, 4091 (1995).
- [5] C. Monroe, D. M. Meekhof, B. E. King, W. M. Itano, and D. J. Wineland, *Demonstration of a Fundamental Quantum Logic Gate*, Physical Review Letters **75**, 4714 (1995).
- [6] R. Blatt, H. Häffner, C. F. Roos, C. Becher, and F. Schmidt-Kaler, *Ion Trap Quantum Computing with Ca+ Ions*, in *Experimental Aspects of Quantum Computing*, edited by H. O. Everitt (Springer US, Boston, MA, 2005), pp. 61–73.
- [7] C. D. Bruzewicz, J. Chiaverini, R. McConnell, and J. M. Sage, *Trapped-Ion Quantum Computing: Progress and Challenges*, Applied Physics Reviews **6**, 021314 (2019).

- [8] H. Häffner, S. Gulde, M. Riebe, G. Lancaster, C. Becher, J. Eschner, F. Schmidt-Kaler, and R. Blatt, *Precision Measurement and Compensation of Optical Stark Shifts for an Ion-Trap Quantum Processor*, Physical Review Letters **90**, 143602 (2003).
- [9] F. Schmidt-Kaler et al., *How to Realize a Universal Quantum Gate with Trapped Ions*, Applied Physics B **77**, 789 (2003).
- [10] D. Kielpinski, C. Monroe, and D. J. Wineland, *Architecture for a Large-Scale Ion-Trap Quantum Computer*, Nature **417**, 709 (2002).
- [11] F. Schmidt-Kaler, S. Gulde, M. Riebe, T. Deuschle, A. Kreuter, G. Lancaster, C. Becher, J. Eschner, H. Häffner, and R. Blatt, *The Coherence of Qubits Based on Single Ca+ Ions*, Journal of Physics B: Atomic, Molecular and Optical Physics **36**, 623 (2003).
- [12] T. Ruster, C. T. Schmiegelow, H. Kaufmann, C. Warschburger, F. Schmidt-Kaler, and U. G. Poschinger, *A Long-Lived Zeeman Trapped-Ion Qubit*, Applied Physics B **122**, 254 (2016).
- [13] M. Malinowski, *Unitary and Dissipative Trapped-Ion Entanglement Using Integrated Optics*, Doctoral thesis, ETH Zurich, 2021.
- [14] V. E. Baranova, P. F. Baranov, S. V. Muravyov, and S. V. Uchaikin, *The Production of a Uniform Magnetic Field Using a System of Axial Coils for Calibrating Magnetometers*, Measurement Techniques **58**, 550 (2015).
- [15] C. Hugon, F. D'Amico, G. Aubert, and D. Sakellariou, *Design of Arbitrarily Homogeneous Permanent Magnet Systems for NMR and MRI: Theory and Experimental Developments of a Simple Portable Magnet*, Journal of Magnetic Resonance **205**, 75 (2010).
- [16] S. K. Ghosh, V. Thakur, and S. Roy Chowdhury, *Design and Simulation of Helmholtz Coil and Maxwell Coil for Low Cost and Low Magnetic Field MRI Machine*, Advanced Materials Proceedings **2**, 802 (2017).
- [17] X. Zhu, C. Liu, H. Su, Y. Miao, and H. Cheng, *Design of Improved Four-Coil Structure with High Uniformity and Effective Coverage Rate*, Heliyon **9**, e15193 (2023).
- [18] R. Bjørk, A. Smith, and C. R. H. Bahl, *Analysis of the Magnetic Field, Force, and Torque for Two-Dimensional Halbach Cylinders*, Journal of Magnetism and Magnetic Materials **322**, 133 (2010).
- [19] C. R. Fernandes, J. O. Ventura, and D. J. Silva, *Rod Mangle Rotation Patterns for Adjustable Magnetic Field Generation*, Journal of Magnetism and Magnetic Materials **565**, 170227 (2023).
- [20] H. Soltner and P. Blümller, *Dipolar Halbach Magnet Stacks Made from Identically Shaped Permanent Magnets for Magnetic Resonance*, Concepts in Magnetic Resonance Part A **36A**, 211 (2010).
- [21] A. Walther, U. Poschinger, F. Ziesel, M. Hettrich, A. Wiens, J. Welzel, and F. Schmidt-Kaler, *Single Ion as a Shot-Noise-Limited Magnetic-Field-Gradient Probe*, Physical Review A **83**, 062329 (2011).

- [22] E. D. Black, *An Introduction to Pound-Drever-Hall Laser Frequency Stabilization*, American Journal of Physics **69**, 79 (2001).
- [23] L.-S. Ma, P. Jungner, J. Ye, and J. L. Hall, *Delivering the Same Optical Frequency at Two Places: Accurate Cancellation of Phase Noise Introduced by an Optical Fiber or Other Time-Varying Path*, Optics Letters **19**, 1777 (1994).
- [24] N. Darkwah-Oppong, *Cancelation of Optical Phase Noise Induced by an Optical Fiber*, Semester thesis, ETH Zurich, 2015.
- [25] A. Sotirova, *A Michelson Interferometer for Vibration Measurements, Fibre Noise Cancellation Setup, Study of Ion Trap Loading Mechanisms*, Semester thesis, ETH Zurich, 2018.
- [26] F. M. Leupold, *Bang-Bang Control of a Trapped-Ion Oscillator*, Doctoral thesis, ETH Zurich, 2015.
- [27] D. T. C. Allcock et al., *Implementation of a Symmetric Surface-Electrode Ion Trap with Field Compensation Using a Modulated Raman Effect*, New Journal of Physics **12**, 053026 (2010).
- [28] Z. D. Romaszko, S. Hong, M. Siegele, R. K. Puddy, F. R. Lebrun-Gallagher, S. Weidt, and W. K. Hensinger, *Engineering of Microfabricated Ion Traps and Integration of Advanced on-Chip Features*, Nature Reviews Physics **2**, 285 (2020).
- [29] K. K. Mehta, C. Zhang, M. Malinowski, T.-L. Nguyen, M. Stadler, and J. P. Home, *Integrated Optical Multi-Ion Quantum Logic*, Nature **586**, 533 (2020).
- [30] J. M. D. Coey, *Permanent Magnet Applications*, Journal of Magnetism and Magnetic Materials **248**, 441 (2002).
- [31] O. Cugat, P. Hansson, and J. M. D. Coey, *Permanent Magnet Variable Flux Sources*, IEEE Transactions on Magnetics **30**, 4602 (1994).
- [32] J. Mallinson, *One-Sided Fluxes - A Magnetic Curiosity?*, IEEE Transactions on Magnetics **9**, 678 (1973).
- [33] R. Bjørk, *The Ideal Dimensions of a Halbach Cylinder of Finite Length*, Journal of Applied Physics **109**, 013915 (2011).
- [34] C. Z. Cooley, M. W. Haskell, S. F. Cauley, C. Sappo, C. D. Lapierre, C. G. Ha, J. P. Stockmann, and L. L. Wald, *Design of Sparse Halbach Magnet Arrays for Portable MRI Using a Genetic Algorithm*, IEEE Transactions on Magnetics **54**, 5100112 (2018).
- [35] B. de Vos, R. F. Remis, and A. G. Webb, *An Integrated Target Field Framework for Point-of-Care Halbach Array Low-Field MRI System Design*, Magnetic Resonance Materials in Physics, Biology and Medicine **36**, 395 (2023).
- [36] F. Gao and L. Han, *Implementing the Nelder-Mead Simplex Algorithm with Adaptive Parameters*, Computational Optimization and Applications **51**, 259 (2012).
- [37] J. A. Nelder and R. Mead, *A Simplex Method for Function Minimization*, The Computer Journal **7**, 308 (1965).
- [38] *Available Grades of Samarium Cobalt SmCo Magnet*, Stanford Magnets (n.d.).

- [39] *How Does Temperature Affect Samarium Cobalt Magnets?*, Stanford Magnets (2020).
- [40] M. Ortner and L. G. Coliado Bandeira, *Magpylib: A Free Python Package for Magnetic Field Computation*, SoftwareX **11**, 100466 (2020).
- [41] P. Malagò, F. Slanovc, S. Herzog, S. Lumetti, T. Schaden, A. Pellegrinetti, M. Moridi, C. Abert, D. Suess, and M. Ortner, *Magnetic Position System Design Method Applied to Three-Axis Joystick Motion Tracking*, Sensors **20**, 6873 (2020).
- [42] R. Beiranvand, *Analyzing the Uniformity of the Generated Magnetic Field by a Practical One-Dimensional Helmholtz Coils System / Review of Scientific Instruments / AIP Publishing*, (n.d.).
- [43] I. McBean, *19 - Manufacturing Technologies for Key Steam Turbine Components*, in *Advances in Steam Turbines for Modern Power Plants (Second Edition)*, edited by T. Tanuma (Woodhead Publishing, 2022), pp. 475–487.
- [44] N. Taran, V. Rallabandi, D. M. Ionel, P. Zhou, M. Thiele, and G. Heins, *A Systematic Study on the Effects of Dimensional and Materials Tolerances on Permanent Magnet Synchronous Machines Based on the IEEE Std 1812*, IEEE Transactions on Industry Applications **55**, 1360 (2019).
- [45] S. Zarate, A. Egea, G. Almandoz, A. McCloskey, U. Galfarsoro, and A. Urdangarin, *A Study of the Effects of the Magnetization Tolerance in the Manufacturing Process on Permanent Magnet Synchronous Machines*, in *2020 10th International Electric Drives Production Conference (EDPC)* (2020), pp. 1–8.
- [46] M. Beetz, *Basics: What Is the Cogging Torque?*, Baumüller (2021).
- [47] *Dimension Tolerance and Sizes That Can Be Made*, (n.d.).
- [48] *Properties of Samarium Cobalt Magnets*, Master Magnetics (n.d.).
- [49] M. T. Villén, M. G. Cañete, E. Martín, M. P. Comech, and C. Lozano, *Manufacturing Tolerances Influence on Permanent Magnet Synchronous Generator (PMSG) Performance*, in (2016).
- [50] *Neodymium Magnets (NdFeB)*, Arnold Magnetic Technologies (n.d.).
- [51] *Available Samarium Cobalt Magnet Grades / Dura Magnetics*, (2014).
- [52] J. E. Greivenkamp, *Field Guide to Geometrical Optics* (2004).